Searching for exotic Higgs bosons at the LHC

Gautam Bhattacharyya,[1,4,*] Siddharth Dwivedi,[2,5,†] Dilip Kumar Ghosh,[3,‡] Gourab Saha,[1,4,§] and Subir Sarkar[1,4,‖]

[1]*Saha Institute of Nuclear Physics, 1/AF Bidhan Nagar, Kolkata 700064, India*
[2]*Institute of Physics, P.O. Sainik School, Sachivalaya Marg, Bhubaneswar 751005, India*
[3]*School of Physical Sciences, Indian Association for the Cultivation of Science, 2A and 2B, Raja S.C. Mullick Road, Kolkata 700032, India*
[4]*Homi Bhabha National Institute, Training School Complex, Anushaktinagar, Mumbai 400094, India*
[5]*Krea University, 5655, Central Expressway, Sri City, Andhra Pradesh 517646, India*

(Received 15 June 2022; accepted 3 September 2022; published 22 September 2022)

We analyze in a model independent way the possibilities of digging out neutral exotic Higgs states, should they exist endowed with unconventional couplings with ordinary matter and gauge fields, at the 14 TeV run of the Large Hadron Collider, adding some comparative studies for 13.6 and 13 TeV runs. Flavor models, based on some discrete symmetry groups, with extended scalar sectors are known to yield exotic spin-0 states, both *CP*-even and *CP*-odd, with purely flavor off-diagonal Yukawa couplings. The gauge interaction of one such *CP*-even state is also unusual that, unlike the Standard Model Higgs boson, it does not couple to gauge boson pairs. Such unconventional properties immune these exotic states from receiving traditional collider and electroweak constraints, and hence those states could be light. Without committing to any specific model, exploiting their peculiar Yukawa and gauge properties, we explore the discovery potential of those exotic Higgs states through some interesting topologies by figuring out some specific kinematic variables that suppress the backgrounds.

DOI: 10.1103/PhysRevD.106.055032

I. INTRODUCTION

Ever since the ATLAS and CMS Collaborations of the CERN LHC discovered the 125 GeV Higgs boson, thus completing the particle spectrum of the Standard Model (SM), the hunters of physics beyond the SM have intensified their searches for any other Higgs-like boson(s). Indeed, there are motivations to hypothesize an underlying extended scalar sector. One of them is the role of additional scalars in facilitating explanation to the flavor problem. Specifically, discrete flavor symmetries have been successfully employed to explain the quark and lepton masses and mixing [1–3]. The byproducts are no less interesting either. With enlarged scalar spectra, many of these flavor models contain exotic spin-0 states endowed with apparently weird couplings to fermions and gauge bosons. Exploiting those unconventional couplings, how to dig those exotic scalar (pseudoscalar) states out of the debris of the 14 TeV LHC is the subject matter of the present paper.

Although our approach is sufficiently model independent, to set up the context, we start our discussion with a reference to a class of flavor models based on the group S_3 introduced in [4]. These models contain enlarged scalar sectors with nonstandard couplings to fermions and gauge bosons. S_3 is the smallest non-Abelian discrete group generating the symmetry of an equilateral triangle. It has two singlet ($\underline{1}$, $\underline{1}'$) and one doublet ($\underline{2}$) irreducible representations. The doublet representation facilitates maximal mixing, and together with the two inequivalent singlets, S_3 can satisfactorily reproduce the fermion masses and mixing. However, what plays a crucial role in these explanations is the presence of three copies of SU(2) doublet Higgs bosons, $\phi_{1,2,3}$, out of which $\phi_{(1,2)}$ form an S_3 doublet and ϕ_3 remains a singlet. A rich scalar spectrum emerges, with three *CP*-even and two *CP*-odd neutral, plus two sets of charged scalars. The details of the minimization of the potential, mass spectra of the scalars (pseudoscalars) and their couplings to the gauge and matter fields may be found in [5,6]. One of the *CP*-even neutral scalars turns out to be the SM Higgs, which we denote by h_{125}. Of the nonstandard states, except a *CP*-even state (H) and a *CP*-odd state (χ), the rest may be considered to be sufficiently heavy having couplings to the gauge and matter fields resembling those in the two-Higgs doublet

*gautam.bhattacharyya@saha.ac.in
†siddharth.d@iopb.res.in
‡tpdkg@iacs.res.in
§gourab.saha@saha.ac.in
‖subir.sarkar@cern.ch

models. With this background, we may forget any model specific details of the scalar spectrum, except concentrating on two peculiar properties of H and χ, which we shall discuss shortly. We also point out that $\Delta(27)$, as the smallest group which provides a source of geometric CP violation, also contains a scalar and pseudoscalar having similar properties [7], see also [3,8]. In this paper we investigate, for the first time, how one can exploit the peculiar behavior of H and χ towards the gauge and matter fields to detect those exotic states at the upcoming 14 TeV run of the LHC.

To propel our discussion this far, we had to draw inspiration from the flavor models. From now onward, we do not appeal to any specific model, as we know that a large class of well-motivated flavor models, which contain three Higgs doublets, carry such exotic scalar (pseudoscalar) states. In fact, from the point of view of an unbiased experimental searches, we merely assume that some underlying scalar sector, regardless of its origin, gives us H and χ with the following nonstandard properties:

(i) There are no HVV-type couplings, where $V \equiv W^{\pm}$, Z. The $H\chi Z$ coupling takes the simple form ($q_\mu \equiv$ momentum transfer):

$$H\chi Z: \left(\frac{-ie}{2\sin\theta_W \cos\theta_W}\right) q_\mu.$$

(ii) $H(\chi)$ has only flavor off-diagonal Yukawa couplings. The relevant piece of Yukawa Lagrangian is

$$Y_{ff'}\bar{f}(i\gamma^5)f'H(\chi) + \text{H.c.}$$

To be more specific, $f, f' \equiv e\mu, \mu\tau, e\tau, uc, tc, ut, ds, db, sb$.

Because there is no HVV coupling, neither the LEP2 limit nor the electroweak precision constraints would apply on the mass of H. The pseudoscalar χ does not couple to VV anyway. Moreover, since neither H nor χ has any diagonal Yukawa coupling, the usual LHC constraints do not apply on their masses either. Therefore, both H and χ could be light [5]. Since the choices of their masses would greatly influence the search strategies, we cannot but make a few working assumptions before we start our analyses. We first select a few benchmark points assuming $m_H \approx m_t$, in a way that the top quark does not have a sizable branching fraction into H and a charm quark. Later we extend the range of m_H mostly to the higher side. We assume χ to be sufficiently light, at least much lighter than H. Indeed, any other choices could be equally likely, but the possibility of a not-so-heavy exotic scalar and a lighter pseudoscalar is in conformity with the lore and excitement prevailing in the community for a while. Similarly, the size of the H/χ off-diagonal Yukawa couplings would impact the search strategies.

For any specific flavor symmetry group, those purely off-diagonal Yukawa couplings have a role to play in reproducing the fermion masses and mixing. Studies with the S_3 group have shown that, in Hqq' coupling, one of q and q' has to be necessarily a third generation quark [5,6]. In the present analysis we remain agnostic about this requirement and treat the generations democratically from the perspective of model blind experimental searches. However, we do keep in mind the extremely tight constraints on Hds and χds couplings from $K_L \to \mu e$ decays, specially when we are dealing with H and χ masses of $\mathcal{O}(10-100)$ GeV [9]. To circumvent this, we set the off-diagonal Hds and χds couplings to zero. We now pay attention to the Huc and χuc Yukawa couplings (Y_q^H and Y_q^χ, respectively), each of which will contribute to the $D^0 - \bar{D}^0$ mixing. Although the constraints from this mixing are not as tight as from $K^0 - \bar{K}^0$ or $B_d^0 - \overline{B_d}^0$ mixing, still for $\mathcal{O}(100)$ GeV mediator masses the upper limit on the corresponding Yukawa couplings would be roughly 10^{-4}. Now, tree level meson mixing amplitude goes as $(\frac{Y_q^{H2}}{m_H^2} - \frac{Y_q^{\chi 2}}{m_\chi^2})$, i.e., a scalar and a pseudoscalar contribute with opposite sign (see, e.g., [10]). In the present analysis, we set $Y_q^\chi \approx \frac{m_\chi}{m_H} Y_q^H$, to relax the above stringent constraint from $D^0 - \overline{D^0}$ mixing by one or two orders of magnitude. We arrange for this partial cancellation to take advantage of our model that contains not only a light scalar but simultaneously a light pseudoscalar, both having purely off-diagonal Yukawa couplings. It is important to note that Y_q^H and Y_q^χ need not be strictly tuned to drive home the essential features of our analysis. These couplings will play a significant role in the production of these exotic spin-0 states at the LHC. The off-diagonal couplings involving the top quark would not be so relevant for our analysis.

On the leptonic sector, nonobservation of various lepton flavor violating (LFV) processes, like $\ell_i \to \ell_j \gamma$ (with $\ell_i \equiv \tau$, μ and $\ell_j \equiv \mu$, e), $\mu + N \to e + N$ (i.e., $\mu - e$ conversion) [11], as well as $e^+e^- \to \mu^+\mu^-(\tau^+\tau^-)$ put a very strong limit on the product of LFV Yukawa couplings involving the first two generations (e, μ) as a function of m_χ and m_H. To respect these limits, we set the $He\mu(\tau)$ and $\chi e\mu(\tau)$ Yukawa couplings to tiny values, order 10^{-9}, for the range of m_χ and m_H considered in the present analysis. We are thus left with $\mu^\pm\tau^\mp$ as the dominant leptonic decay mode of $H(\chi)$. With the above in mind, we focus on the LFV signatures of H and χ. To be specific, we focus on two different types of final state topologies: $\tau_h + 3\mu$ and $\tau_h + \mu + 2e$, where τ_h indicates a hadronically decaying τ lepton. We generate the signal events at the leading order for two representative values of m_H and m_χ each by varying the flavor violating Yukawa couplings Y_ℓ and Y_q within their experimentally permissible range. The corresponding SM background events are also generated at the leading order. Finally, we obtain the signal significance using both the cut based and the multivariate analysis encoded in the boosted decision tree (BDT).

The paper is organized in the following way: In Sec. II, we outline the choice of benchmark points for the flavour violating Higgs signal processes. In Secs. III and IV we elaborate the signal and various SM background processes. In Sec. V, we present the simulation set up, perform the collider analysis of the aforementioned two multilepton channels, and compute the sensitivity of the events at the 14 TeV run of the LHC experiment. We also compare how the signal cross sections would alter in the upcoming phase of the 13.6 TeV run of the LHC. We further demonstrate that for the choices of the Yukawa couplings which are on the higher side, the signal cross sections and the significance values corresponding to the already concluded 13 TeV run of the LHC contain enough incentive for this analysis to be taken up by the experimental groups for a detailed investigation. In Sec. VI, we examine the impact of including possible systematic uncertainties on the SM backgrounds for signal benchmarks over an extended range of m_H. Finally we summarize our main findings in Sec. VII.

II. CHOICE OF BENCHMARK POINTS

First, we focus on various quark and lepton flavor violating couplings that are involved in the production and decays of H and χ. The set of new Yukawa couplings that are relevant here are Y_q (i.e., $Y_q^{H,\chi}$) and Y_ℓ ($\ell = \mu, \tau$), where Y_q is responsible for the production of H/χ in $u(\bar{u})\bar{c}(c) \to H/\chi$ processes, while Y_ℓ drives the decay $H/\chi \to \mu^\pm\tau^\mp$. Thus the flavor violating signal cross sections depend upon those two Yukawas (Y_ℓ and Y_q) as well as on m_χ and m_H.

Henceforth, for notational simplicity we shall denote Y_q^H by Y_q. The values of Y_q^χ will be automatically set as $\frac{m_\chi}{m_H} Y_q^H$, as mentioned in the Introduction. We produce signal event samples for four different combinations of (m_H, m_χ), and for each such combination, we take six benchmark values for Y_ℓ and Y_q each, as shown in Table I. Those six values for both Y_ℓ and Y_q are chosen as 0.001,0.003,0.005, 0.007, 0.009, and 0.01. In view of the approximate relation between Y_q^χ and $Y_q^H \equiv Y_q$, the above six values of quark Yukawa couplings are consistent with $D^0 - \bar{D}^0$ mixing constraint.

Thus there are $4 \times 36 = 144$ signal benchmark configurations, and we calculate the signal significance for each of these sample points. The values of m_χ are such that χ can be produced on shell in association with a Z boson from the decay of the heavier scalar H with sufficient phase space [keeping a mass gap $\delta m = (m_H - m_\chi) \sim \mathcal{O}(100)$ GeV], so that the decay products of χ and Z have substantial transverse momenta to satisfy the baseline selection criteria of our analysis. For $m_\chi < 20$ GeV, the χ decay products (μ, τ_h) would be too soft to be detected, while for $m_\chi \simeq (M_Z, M_W)$ the on-shell two-body decay $H \to \chi + Z$ would be kinematically disfavored for our choices of m_H.

TABLE I. Benchmark choices of masses and flavor violating Yukawa couplings.

Mass (GeV)	$m_\chi = 20$	$m_\chi = 60$
$m_H = 160$	$(Y_\ell, Y_q)_{6\times6}$	$(Y_\ell, Y_q)_{6\times6}$
$m_H = 170$	$(Y_\ell, Y_q)_{6\times6}$	$(Y_\ell, Y_q)_{6\times6}$

In addition to the above mentioned representative signal benchmark points, we also consider an extended scenario by varying m_H from 140 to 500 GeV, and demonstrate the effects of systematic uncertainties on signal significance. While doing this analysis, we keep the range of m_χ and Yukawa couplings the same as before.

III. SIGNAL PROCESSES

Having discussed the constraints on our model parameters, we are set to explore the collider signatures of H and χ at $\sqrt{s} = 14$ TeV LHC run. We consider two processes **S1**(**S2**), where $\chi Z(HZ)$ pair is produced on shell. Subsequently, the nonvanishing LFV Yukawa coupling Y_ℓ induces $\chi(H)$ decay into $\mu^\pm\tau^\mp$ pairs. From the decay of the Z boson, we pick up only the $\mu^+\mu^-/e^+e^-$ final states.

$$\textbf{S1}: pp \to \chi(\to \mu^\pm\tau^\mp)Z(\to e^+e^-/\mu^+\mu^-),$$
$$\textbf{S2}: pp \to H(\to \mu^\pm\tau^\mp)Z(\to e^+e^-/\mu^+\mu^-).$$

In the subsequent discussion, whenever we refer to **S1** and/or **S2** cross section(s), we imply the relevant boson production cross section(s) × their branching ratios into multilepton final satte. In Fig. 1, we display the **S1** and **S2** signal processes. Depending upon the charged lepton flavor from the Z decay, **S1** and **S2** have the following lepton flavors in their respective final states: (*a*) $\tau_h + 3\mu$ and (*b*) $\tau_h + \mu + 2e$. Treating electron and muon on the same footing, we are eventually led to $\tau_h + 3\ell_0$, $(\ell_0 = e, \mu)$ as our final signal topology. To simulate the signal we first implement the LFV Lagrangian in FeynRules [12] to generate a Universal FeynRules Output to be interfaced with the event generator. We then generate the signal processes using MadGraph5_aMC@NLO [13] at the leading order (LO). All the SM background events have been generated using MadGraph5_aMC@NLO. For the calculation of both the signal and the SM background processes we employ NN23LO1 as the parton distribution function [14]. The τ decays are simulated by the TAUOLA package integrated in MadGraph5_aMC@NLO. The parton level events are then passed through PYTHIA 8 [15] for parton showering, hadronization and the resulting events are finally processed through the fast detector simulation package DELPHES 3 [16] using the default CMS card. DELPHES uses the anti-k_T algorithm [17] to perform jet clustering using the FastJet package [18]. The respective tagging efficiencies for the b- and τ-tagged jets have been parametrically incorporated within DELPHES. We produce signal samples for the

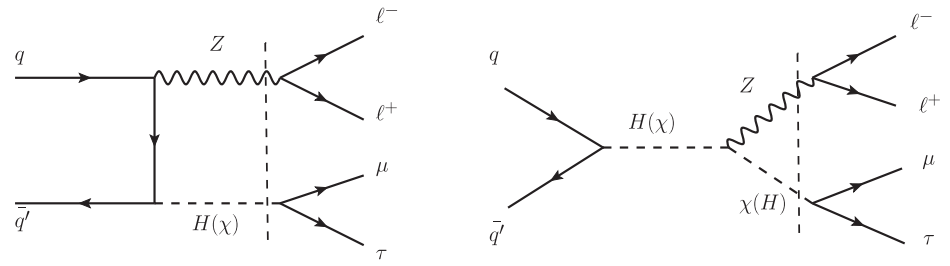

FIG. 1. Feynman diagrams for the signal processes. The dashed vertical lines are indications of the on-shell production of H/χ in association with Z, and their subsequent decays into $\mu^{\pm}\tau^{\mp}$ and $\mu^+\mu^-/e^+e^-$, respectively.

benchmark choices in Table I, which means that 144 signal benchmark points are generated, and for each such point we estimate the signal significance.

In Fig. 2 we exhibit the variation of the cross sections for **S1** and **S2** as a function of Y_ℓ for different values of Y_q for the choices, (m_χ, m_H) in GeV: (a) (20,160) and (b) (60,170), respectively. We generate all the signal processes keeping the default MadGraph settings. A few comments on some gross features of Fig. 2 are in order, as these will have important bearing in planning the collider analysis. The **S1** and **S2** cross sections increase with Y_q and Y_ℓ. This is expected as Y_q boosts the production while Y_ℓ facilitates the decays of the exotic states into $\mu^{\pm}\tau^{\mp}$. The cross section for $S1$ $(pp \to \chi Z)$ is roughly five orders of magnitude larger than that of $S2$ $(pp \to HZ)$ simply because of kinematics $(m_\chi \ll m_H)$. Henceforth, we consider only the **S1** process in our detailed collider analysis. With this signal topology in mind, we generate appropriate SM backgrounds.

Before leaving this section, we point out that there exists another competitive channel worth exploring, which is

$$pp \to t\bar{t}, t \to bW, \bar{t} \to u(c)\chi(H). \tag{3.1}$$

Here, one of the top quarks decays into Wb via the SM gauge coupling, while the other can decay into $u(c)\chi$ or $u(c)H$ induced by off-diagonal $H(\chi)tu$ or $H(\chi)tc$ couplings, followed by $W \to l\nu_l/jj(l = e, \mu, \tau)$ and $\chi \to \mu\tau$. The cross section for this process is of the same order of magnitude as that for the associated production channel (**S1**). The **S1** channel has two distinct advantages over the channel in Eq. (3.1) arising from the higher lepton multiplicity in the final state and from the availability of an invariant mass (M_Z) construction from opposite sign same flavor (OSSF) lepton pairs to be used as an efficient discriminator against the backgrounds. However, the process in Eq. (3.1) merits a separate dedicated analysis.

A few comments on why we have looked for χ, not singly but in association with Z, are in order. First, from an experimental point of view, looking for an isolated χ decaying resonantly to two-body (μ, τ) final state would be extremely challenging. In spite of its large cross section, the signal will be completely swamped by the background. QCD backgrounds for low mass events will be overwhelming, and also $Z \to \tau^+\tau^-$ with one τ decaying to μ would mimic the signal, specifically for large m_χ, with uncontrollably large statistics. It is therefore better to focus on the associated process. Second, from the motivational point of view, we actually probed a scenario which provides

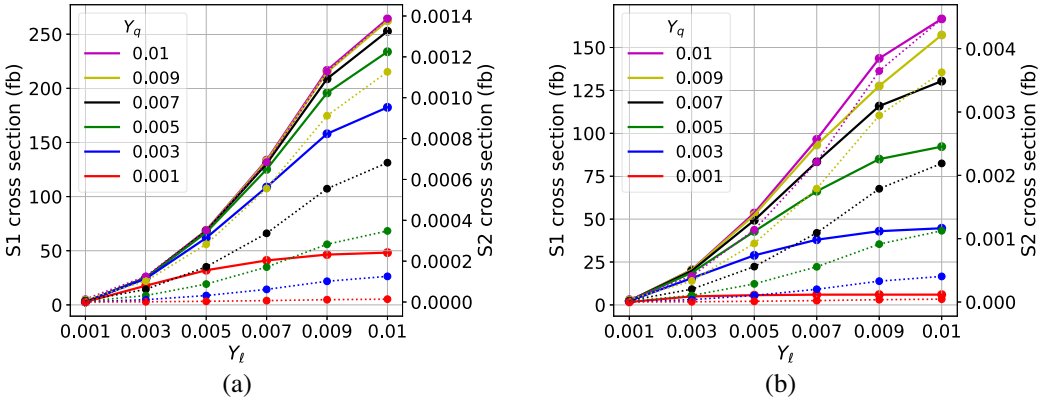

FIG. 2. Signal process cross sections, i.e., production cross sections × branching ratios at $\sqrt{s} = 14$ TeV, as a function of Y_l for fixed values of Y_q. Solid lines are for **S1** and dotted ones are for **S2**. The left panel (a) is for $(m_\chi, m_H) = (20, 160)$ GeV, while the right panel (b) is for (60,170) GeV.

a $H\chi Z$ interaction, as stressed in the Introduction. Thus a (χZ) final state, i.e., production of χ in association with Z which is easy to reconstruct with a potential to reign over the background, arises naturally through the Feynman diagrams shown in Fig. 1.

IV. BACKGROUNDS

There are several SM processes which constitute the background by imitating the final state $(1\tau^{\pm} + 3\ell_0)$. For all backgrounds, we use either the next-to-leading order (NLO) cross section if they are available in the literature or use the LO cross sections (weighted by the k factor) employing MadGraph. The dominant backgrounds arise from $ZZ(\to 4l^{\pm})+$ up to 2 jets, $W^{\pm}Z(\to 3l^{\pm})+$ up to 2 jets, $t\bar{t}Z(\to l^+l^-)+$ up to 2 jets, WWZ (with all possible decays of W and Z), and $t\bar{t}+1$ jet with both top quarks decaying leptonically. The background from WZZ is subdominant, while negligible contributions arise from the backgrounds $Z(\to l^+l^-)+$ up to 2 jets, ZZZ, WWW, $W^{\pm}Z+$ up to 2 jets (with $W^{\pm} \to jj, Z \to l^+l^-$), $t\bar{t}W^{\pm}+$ up to 2 jets and $ggF/VBF \to h_{125} \to ZZ^* \to 4l^{\pm}$. The LO backgrounds $ZZ+\text{jets}$, $WZ(3l)+\text{jets}$, $t\bar{t}Z+\text{jets}$ are normalized to NLO by the k factors 1.62 [19], 1.88 [19], and 1.4 [20], respectively. For $t\bar{t}+\text{jets}$ background, we use the N^{3}LO cross section from [21]. Rest of the SM background processes are estimated at LO only.

V. ANALYSIS

In this section we perform a detailed Monte Carlo analysis for the signal topologies that consist of three charged leptons ($e^{\pm}e^{\mp}\mu^{\pm}$ or $\mu^{\pm}\mu^{\mp}\mu^{\pm}$) and one tau-tagged jet (τ_h). We divide the whole event selection procedure into two steps: (i) baseline selection and (ii) signal extraction.

A. Baseline selection

Charged particles (leptons and jets) produced in any hard scattering process at the LHC may not be always visible due to the finite size of the detector and the requirement of minimum energy to trigger. Hence, we first apply a set of acceptance cuts (C0) as shown in Table II on all the charged leptons and jets so that they can be observed at various subcomponents of the CMS detector. Next, we construct various kinematic observables and study their distributions for both the signal and backgrounds. Based on the final state composition and distinguishable features of the distributions of kinematic variables for the signal and backgrounds we apply preselection cuts (C1–C6) to loosely suppress the background contributions.

C0: This consists of basic selection criteria for e, μ, τ and jets. We use the following set of kinematic variables: (i) transverse momentum p_T, (ii) pseudorapidity η, and (iii) angular separation between two objects, ΔR, where $\Delta R_{ij} = \sqrt{(\Delta\eta)^2 + (\Delta\Phi)^2}$ is defined in terms of the azimuthal angular separation $(\Delta\Phi)$ and pseudorapidity difference $(\Delta\eta)$ between two objects i and j. The threshold values of these variables are shown in Table II.

TABLE II. Summary of acceptance cuts.

Objects	Selection cuts
e	$p_T > 10$ GeV, $\lvert\eta\rvert < 2.5$, $\Delta R_{e\mu} > 0.4$
μ	$p_T > 10$ GeV, $\lvert\eta\rvert < 2.4$, $\Delta R_{e\mu} > 0.4$
τ_h	$p_T > 20$ GeV, $\lvert\eta\rvert < 2.4$, $\Delta R_{\tau,e\mu} > 0.4$
Jet	$p_T > 20$ GeV, $\lvert\eta\rvert < 4.7$, $\Delta R_{\text{jet},e\mu} > 0.4$

C1: The signal has a Z boson decaying to a pair of OSSF leptons (e, μ). To ensure the presence of one Z boson, we select events with an invariant mass $M_{\ell_0^+\ell_0^-}$ close to the Z peak by demanding $|M_{\ell_0^+\ell_0^-} - M_Z| < 10$ GeV, where M_Z is the true Z mass. The same cut has been used to suppress the SM di-Z contribution by rejecting events having more than one Z boson.

C2: We look only for the leptonic decay of χ, i.e., $\chi \to \mu^{\pm} + \tau^{\mp}$. So, we require at least one μ to be present in the selected events.

C3: Based on C1 and C2, we demand the presence of three charged leptons in the final state, one μ from χ decay and $e^+e^-/\mu^+\mu^-$ from Z decay.

C4: One of the decay products of χ is a τ lepton, and we choose to work with the τ that decays in hadronic mode. We require at least one τ jet (τ_h) to be present in the final state.

C5: Now we have three muons (with one OSSF pair), or, one muon + one OSSF electron pair in the final state, along with the τ jets. The μ which is not a decay product of Z, paired with a τ_h of opposite charge. Together they are perceived to have arisen from χ decay. This μ is denoted as μ' hereafter.

C6: The signal final state is free from b jets. So, we impose a b jet veto in our baseline selection to suppress the top quark enriched SM backgrounds.

In Table III we present the effective cross section (fb) after acceptance and successive pre-selection cuts, C1 to C6, for both the signal and background events, and in the last column we show the corresponding number of events at an integrated luminosity of 300 fb^{-1}. One should note that we only show a few representative benchmark points for the signal samples. One can see from Table III that after the baseline selection cuts, major SM background processes turn out to be $ZZ(4l)+\text{jets}$ and $W^{\pm}Z(3l)+\text{jets}$, followed by $t\bar{t}Z+\text{jets}$. The $ZZ(4l)+\text{jets}$ process has two Z bosons decaying to leptons of any flavor. The hadronic branching ratio of τ is 64.8% [22] and the detection efficiency of such a τ is 60% as considered in DELPHES. The combined effect of these two is the main reason for getting low signal efficiency of C4 cut. In Fig. 3 we show normalized

TABLE III. The signal and SM background effective cross sections (fb) after each successive baseline cut (C0–C6) and final event yields for $\mathcal{L} = 300$ fb^{-1} at 14 TeV LHC run. Signal event samples are generated for a few representative values of m_χ and m_H (in GeV) and for a range of Y_ℓ and Y_q. Signal cross sections are calculated at LO, $t\bar{t}+$ jets cross sections at N^{3}LO, while the other SM backgrounds are estimated at NLO.

Samples	$\sigma_{\text{prod}}\times$ BR (fb)	Effective cross sections (fb)							Events (300 fb^{-1})
		C0	C1	C2	C3	C4	C5	C6	
Signal									
$(m_\chi, m_H) - (Y_\ell, Y_q)$									
$(20, 160) - (0.003, 0.001)$	2.8	2.708	0.747	0.620	0.367	0.037	0.036	0.035	10.47
$(20, 160) - (0.005, 0.005)$	66.89	64.799	17.894	14.865	8.809	0.895	0.874	0.845	253.53
$(20, 160) - (0.009, 0.007)$	132.82	128.59	35.472	29.428	17.403	1.818	1.772	1.725	517.6
$(20, 170) - (0.003, 0.001)$	2.3	2.238	0.627	0.522	0.310	0.037	0.036	0.035	10.54
$(20, 170) - (0.005, 0.005)$	55.44	53.945	15.278	12.748	7.493	0.89	0.878	0.845	253.47
$(20, 170) - (0.009, 0.007)$	110.16	107.19	29.999	25.015	14.718	1.772	1.737	1.667	500.18
$(60, 160) - (0.003, 0.001)$	2.98	2.89	0.701	0.637	0.464	0.079	0.077	0.074	22.3
$(60, 160) - (0.005, 0.005)$	53.55	51.914	12.508	11.361	8.297	1.38	1.353	1.304	391.08
$(60, 160) - (0.009, 0.007)$	114.44	110.88	26.875	24.375	17.768	2.981	2.921	2.82	845.94
$(60, 170) - (0.003, 0.001)$	2.29	2.231	0.58	0.523	0.368	0.066	0.065	0.063	18.75
$(60, 170) - (0.005, 0.005)$	42.83	41.717	10.802	9.737	6.887	1.203	1.181	1.142	342.55
$(60, 170) - (0.009, 0.007)$	93.2	90.751	23.49	21.222	14.988	2.669	2.619	2.521	756.18
SM backgrounds									
$Z+$ jets	6.33×10^6	6.32×10^6	2.9×10^5	1.8×10^5	12.74	0.11	0	0	0
$t\bar{t}+$ jets (21)	1.09×10^5	1.09×10^5	1522.34	967.5	3.58	0.1	0.03	0.03	9.11
$t\bar{t}W^\pm+$ jets	253.8	253.78	1.125	0.779	0.22	0.013	0.005	0.001	0.43
$t\bar{t}Z+$ jets	240.3	240.3	57.68	39.79	11.86	1.193	0.536	0.141	42.15
$W^\pm Z+$ jets (31)	2273	2263.6	849.86	614.95	389.99	3.67	1.207	1.144	343.17
$W^\pm Z+$ jets (21)	4504	4496.3	1220.17	769.65	0.18	0.007	0.002	0.002	0.55
$ZZ+$ jets (41)	187.3	186.46	71.86	51.86	26.89	2.106	1.286	1.254	376.34
(GGF) ZZ (4l)	14.82	14.476	2.16	1.68	0.92	0.01	0.003	0.002	0.73
(VBF) ZZ (4l)	2.211	2.21	0.32	0.24	0.13	0.003	0.001	0.001	0.28
WWW	236.2	236.07	0.6	0.39	0.08	0	0	0	0
WWZ	188.9	188.75	4.84	3.24	1.0	0.07	0.038	0.034	10.2
WZZ	63.76	63.65	3.036	2	0.46	0.025	0.01	0.009	2.64
ZZZ	15.8	15.73	1.08	0.69	0.06	0.007	0.004	0.003	0.95

distributions of a few kinematic variables for the signal and two most dominant classes of SM backgrounds after the baseline selection. For signal events, we choose two benchmark mass points $(m_\chi, m_H) = (20, 160)$ and (60,170) GeV. The dominant background processes are $VV+$ jets $(VV = WZ, ZZ)$ and $ttV+$ jets $(V = W,\ Z)$. These variables shown in Fig. 3 would play a significant role in the signal discrimination both in the cut based and the multivariate analyses. The major source of $\not{E}_T$ in the signal is from neutrino produced in the hadronic τ decay. One should note that undetected charged leptons and/or τ jet are likely to make small contributions to the missing transverse energy. Since the choices for the mass m_χ of the parent particle in the two cases are not very different, we do not expect any significant change in the $\not{E}_T$ distributions for two different signal benchmark points, as depicted in Fig. 3(c). The transverse momentum (p_T) of μ' and τ_h show similar behavior as $\not{E}_T$, as shown in Figs. 3(a) and 3(b), respectively. All the three distributions show that the SM backgrounds are harder than the signal contributions. We also show the distribution of ΔR between the two OSSF leptons, i.e., the decay products of Z in Fig. 3(d).

At the end of the baseline selection, we attempt to reconstruct m_χ by combining the four momenta of its decay products, μ' and τ_h. Unfortunately, this prescription does not work in this case because one cannot fully reconstruct the four momentum of τ as the hadronic decay of tau is associated with a missing neutrino. Nevertheless, one can still get some idea about m_χ using a different kinematic variable, transverse mass (m_T), defined in terms of p_T of μ', τ_h, and $\not{E}_T$. In doing so, we also assume that the aforementioned neutrino is the only source of $\not{E}_T$ for

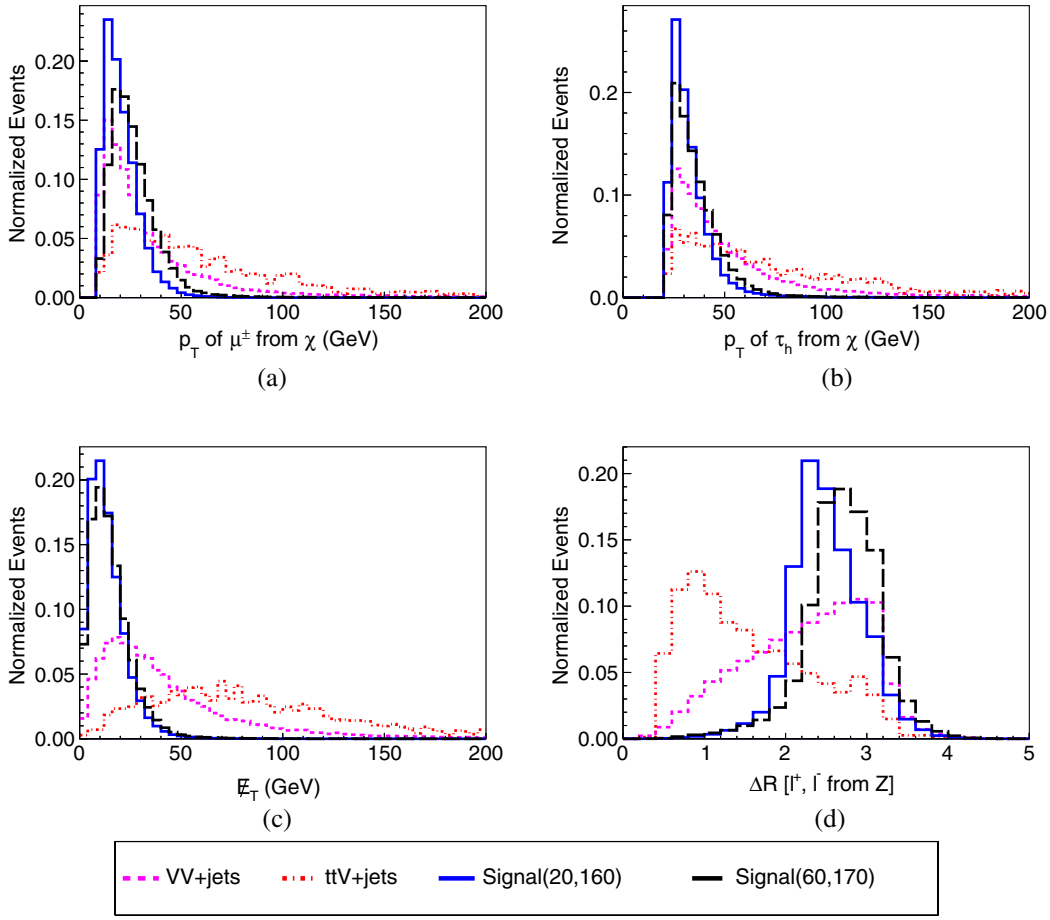

FIG. 3. Distributions of some kinematic variables, (a) p_T of μ (i.e., μ') from χ, (b) p_T of τ_h from χ, (c) $\not{E}_T$, and (d) ΔR between the two OSSF leptons from Z, after baseline selection are shown for two representative mass points (m_χ, m_H) in GeV: (20,160) [solid blue] and (60,170) [black long dashed]. For comparison, distributions of the same kinematic variables are shown for two major SM backgrounds, namely, $VV+\text{jets}$ [magenta small dashed] and $ttV+\text{jets}$ [red dash dotted], where $V = W^\pm, Z$.

signal events. For a two body decay, the transverse mass is defined as

$$m_T(a,b) = \sqrt{2 \times p_T^a \times p_T^b \times (1 - \cos(\Delta\Phi^{a,b}))}, \quad (5.1)$$

where a and b are the final decay products and $\Delta\Phi^{a,b} = |\Phi_a - \Phi_b|$. For the final state considered here, the transverse mass variable for the system comprising μ', τ_h, and $\not{E}_T$ is constructed as [23,24]

$$m_T(\mu', \tau_h, \not{E}_T) = \sqrt{m_T^2(\mu', \not{E}_T) + m_T^2(\tau_h, \not{E}_T) + m_T^2(\mu', \tau_h)}. \quad (5.2)$$

In Fig. 4(a) we show normalized transverse mass distributions for both the signal and the SM backgrounds. Here we clearly see the presence of reconstructed χ around 20 GeV and 60 GeV. The peak of the signal distribution is very well separated from the SM backgrounds $VV+\text{jets}$ as long as m_χ is not close to either M_W or M_Z. We observe that for $m_\chi = 60$ GeV, there is a substantial overlap between the signal region and the SM backgrounds $VV+\text{jets}$. Figure 4(b) shows the distribution of collinear mass [25] of the μ', τ_h, and $\not{E}_T$ system, which we explain in the following. The collinear mass technique is useful to reconstruct the mass of a particle decaying to τ and other visible objects. It is assumed that the decay products of τ are boosted in the original direction of τ itself since $m_\tau \ll m_\chi$. Thus the transverse component of the τ neutrino (ν_τ) momentum, p_T^ν, can be estimated by taking the projection of $\not{E}_T$ in the direction of visible τ_h. The definition of the collinear mass is

$$m_{\text{coll}} = \frac{m_{\text{vis}}}{\sqrt{\beta_\tau^{\text{vis}}}}, \quad (5.3)$$

where m_{vis} represents the invariant mass of τ_h and μ', whereas β_τ^{vis} is the fraction of the τ momentum carried by the visible (hadronic) τ decay products (τ_h), i.e., $\frac{p_T^{\tau_h}}{p_T^{\tau_h} + p_T^\nu}$ [26]. The collinear mass exhibits a somewhat better resolution

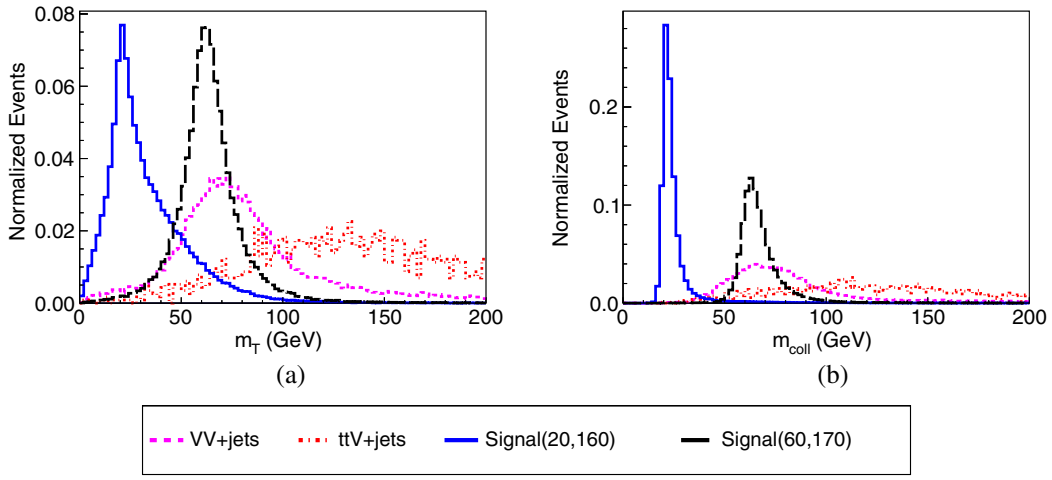

FIG. 4. Distributions of (a) transverse mass (m_T) and (b) collinear mass ($m_{\rm coll}$) of the reconstructed χ after baseline selection.

than the transverse mass distribution. Both distributions affirm the existence of χ in the signal processes. We have performed the exercise to indicate the possibility as well as the limitations of the mass reconstruction procedure in our scenario. We further extend and refine our baseline analysis to cut based and multivariate analyses to obtain the final signal significance $\mathcal{S}$ defined in terms of number of signal and background events S and B as

$$\mathcal{S} = \frac{S}{\sqrt{S+B}}, \tag{5.4}$$

where $S(B)$ can be estimated as $S(B) = \sigma_{S(B)} \times \mathcal{L} \times \epsilon_{S(B)}$, with $\sigma_{S(B)}$, $\mathcal{L}$ and $\epsilon_{S(B)}$ denoting the signal (background) cross section, integrated luminosity and signal (background) selection efficiency, respectively.

B. Signal extraction: Cut-based analysis

In the cut based analysis, we impose a condition of missing energy on top of the baseline selection. As the background can have several sources of $\not{E}_T$, namely, multiple neutrinos, jet energy mismeasurements and mistagged charged leptons, it has a much harder $\not{E}_T$ spectrum compared to the signal. We reject all events with $\not{E}_T > 40$ GeV and this substantially reduces various background contributions.

In Table IV we display the effects of $\not{E}_T$ cut on baseline selected signal and background events, where the last

TABLE IV. Summary of the cut based analysis.

Samples	Baseline cross section (fb)	Effective cross sections (fb) ($\not{E}_T < 40$ GeV)	Events $\mathcal{L} = 300$ fb^{-1}
Signals			
$(m_\chi, m_H) - (Y_\ell, Y_q)$			
$(20, 160) - (0.003, 0.001)$	0.035	0.034	10.2
$(20, 160) - (0.005, 0.005)$	0.845	0.832	249.6
$(20, 160) - (0.009, 0.007)$	1.725	1.697	509.1
$(20, 170) - (0.003, 0.001)$	0.035	0.034	10.2
$(20, 170) - (0.005, 0.005)$	0.845	0.826	247.8
$(20, 170) - (0.009, 0.007)$	1.667	1.64	491.9
$(60, 160) - (0.003, 0.001)$	0.074	0.073	21.9
$(60, 160) - (0.005, 0.005)$	1.304	1.278	383.4
$(60, 160) - (0.009, 0.007)$	2.82	2.762	828.6
$(60, 170) - (0.003, 0.001)$	0.063	0.061	18.3
$(60, 170) - (0.005, 0.005)$	1.142	1.114	334.2
$(60, 170) - (0.009, 0.007)$	2.521	2.445	733.5
SM backgrounds			
$t\bar{t}Z +$ jets	0.141	0.025	7.5
$W^{\pm}Z +$ jets (3l)	1.144	0.423	126.9
$ZZ +$ jets (4l)	1.254	0.816	244.8

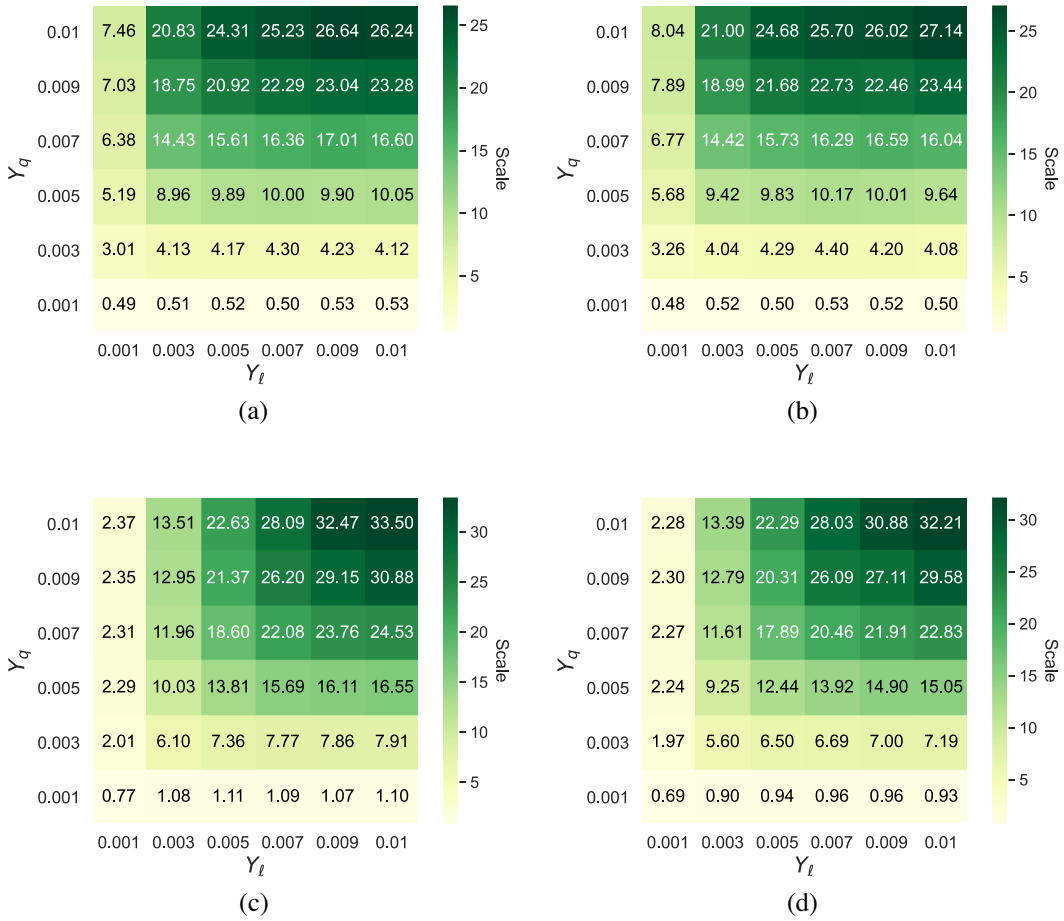

FIG. 5. Significance plots for the four mass benchmark configuration points at $\mathcal{L} = 300$ fb^{-1} following the cut based analysis. The two plots in the upper panel are for (m_χ, m_H) in GeV: (a) (20,160) and (b) (20,170). The lower panel contains the other two mass points, in GeV, (c) (60,160) and (d) (60,170).

column shows the number of signal and background events at $\mathcal{L} = 300$ fb^{-1}. For signal events, we select a few representative benchmark points to show the efficiencies of cut based analysis. In the final signal significance calculation, we use all the signal benchmarks points that are shown in Sec. II.

In Figs. 5(a)–5(d), represent signal significances in the $Y_\ell - Y_q$ Yukawa plane at 14 TeV LHC with $\mathcal{L} = 300$ fb^{-1} corresponding to $(m_\chi, m_H) = (20,160), (20,170), (60,160)$, and (60, 170) GeV, respectively. As can be inferred from the plots, for a given value of m_χ and m_H, the significance increases with increase in Y_ℓ and Y_q. The reason is easy to understand from the functional dependence of the signal cross section on Y_ℓ and Y_q as showcased in Fig. 2. The cut based analysis shows that for all of these four mass benchmark points, the signal significance $\mathcal{S} > 5\sigma$ is achievable for $Y_\ell(Y_q)$ as low as 0.001(0.003). By proper scaling one can easily obtain the signal significance at higher luminosities. For example, by looking at Fig. 5 for $(Y_\ell, Y_q) = (0.001, 0.001)$, we find though that the required luminosity for 5σ significance is above 3000 fb^{-1}, which is beyond the reach of HL-LHC. For the benchmarks with lighter pseudoscalar as shown in Figs. 5(a) and 5(b), we find that the required luminosity for 5σ significance for $(Y_\ell, Y_q) = (0.001, 0.003)$ is $\mathcal{L}_{5\sigma} \sim 800$ fb^{-1}. Similarly, for heavier mass of χ shown in Figs. 5(c) and 5(d), we require $\mathcal{L}_{5\sigma} \sim 1900$ fb^{-1} integrated luminosity to achieve a 5σ significance with the same set of couplings. These clearly indicate that the high luminosity option of the LHC has enough potential to dig out such exotically behaving spin-0 states. Here we point out that for a few values of Y_ℓ and Y_q in Fig. 5, the value of the significance $\mathcal{S}$ remains either the same or gets smaller for the next higher value of either Y_ℓ or Y_q. These anomalies, however, are the results of statistical fluctuation while estimating the signal significance. Also, the signal significance has been estimated using simple cut based analysis where we have considered real physics backgrounds only, neglecting various fake rates and systematic uncertainties associated with various SM background estimations. Hence, these significance values may be considered merely as indicative ones.

TABLE V. List of kinematic variables used in the BDT based analysis.

Variable	Definition
$p_T^{\mu'}$	Transverse momentum of μ'
$p_T^{\tau_h}$	Transverse momentum of the τ_h from χ
$\not{E}_T$	Missing transverse energy
p_T^Z	Transverse momentum of the selected Z candidate
$\Delta R_{l^+l^-}$	ΔR between the OSSF leptons from Z decay
$m_T(\not{E}_T, e/\mu)$	Transverse mass of $\not{E}_T$ and μ'
$\alpha_{\chi,Z}$	Angle between the planes of the pair of μ', τ_h and the pair consisting of two OSSF leptons from Z

C. Signal extraction: Multivariate analysis

It emerged in recent years that the application of multivariate analysis provided better separation between the signal and background than the usual rectangular cut based analysis [27–32]. Inspired by these studies, we proceed to perform the multivariate analysis using the BDT [33] algorithm to explore the possibility of improving the signal significance over the cut based one. In Table V we show the list of input variables used for the training and validation of our BDTs. After the baseline selection, we have trained BDTs separately for the four signal mass points mentioned earlier. We use a simple BDT architecture in the Root TMVA [34] package with the set of parameters as shown in Table VI.

For training and testing of BDTs at each mass configuration, we combine the signal events for all the (Y_ℓ, Y_q) points because there are negligible changes in the shape of the kinematic variables for different combinations of coupling values. We employ a comparable number of signal and background events (about 75% of the latter) to prepare the training dataset, where all the events have been selected randomly. We only consider the two major backgrounds $W^\pm Z(3l) + \text{jets}$ and $ZZ(4l) + \text{jets}$ as shown in Table III. We tune the BDT parameters in Table VI to minimize the over training for optimal performance.

In Fig. 6 we display the distributions of the BDT classifier score for the signal benchmark points (m_χ, m_H): (a) (20, 160), (b) (20, 170), (c) (60,160), and (d) (60,170) GeV, respectively, and two SM backgrounds. We can see from Fig. 6 that for signal benchmarks with both lighter (upper panels) and heavier χ (lower panels), the classifier shows similar performance. The performance of training and the possibility of over fitting can be inferred from the shape of the receiver operating characteristic (ROC) curves as displayed in Fig. 7. From this figure, it is evident that the ROC looks similar for both the training and test samples, which implies very negligible over training in our BDT analysis. The area under the curve (AUC) is a metric to show the performance of a classifier. A complete separation between signal and background would make AUC $= 1$ and here the value is almost 0.93. So, the performance of BDT and negligible overfitting undoubtedly give us the confidence that we proceed further to estimate the final signal significance with $\mathcal{L} = 300$ fb^{-1}.

To get the final significance for all the signal benchmarks we first scale the number of signal and background events with a factor of $\sigma_{S(B)} \times \mathcal{L} \times \epsilon_{S(B)}$ and then we iterate over the BDT scores to get the optimal point corresponding to the maximum significance. In Table VII we only show the performance of two BDT models trained for (m_χ, m_H): (20, 160) and (60, 170) GeV signal processes, respectively. We only tabulate the application of the BDT models on $(Y_\ell, Y_q) = (0.005, 0.005)$ signal coupling benchmark point. The last column of Table VII shows the final yield at $\mathcal{L} = 300$ fb^{-1} and the yield corresponds to the highest value of significance for the scenario under consideration. Keeping the same format of Fig. 5 (cut based), we show the variation of the signal significance $(\mathcal{S})$ as a function of the scalar masses (m_χ, m_H) and Yukawa couplings (Y_ℓ, Y_q) in Fig. 8. The functional dependence of $\mathcal{S}$ on model parameters $(m_\chi, m_H, Y_\ell, Y_q)$ remains the same as in the cut based analysis. From these four panels, one can see that even for a modest value of $Y_q = Y_\ell \sim 0.003(0.005)$, we get $\mathcal{S} \sim 8(14)$ with 300 fb^{-1} data.

D. 14 vs 13.6 vs 13 TeV

It is likely that during 2022–2024, LHC would run at 13.6 TeV and during that period it might collect 150 fb^{-1} data [36].

Eventually in 2027 the center of mass energy might be jacked up to 14 TeV and, subsequently, availability of an

TABLE VI. The list of BDT parameters: definition and values used.

BDT parameters	Description	Value
`NTrees`	Number of trees or nodes	750
`MinNodeSize`	Minimum % of training events required in a leaf node	5%
`MaxDepth`	Max depth of the decision tree allowed	3
`BoostType`	Boosting mechanism to make the classifier robust	AdaBoost [35]
`AdaBoostBeta`	Learning rate for AdaBoost algorithm	0.5
`nCuts`	Number of grid points in variable range used in finding optimal cut in node splitting	20

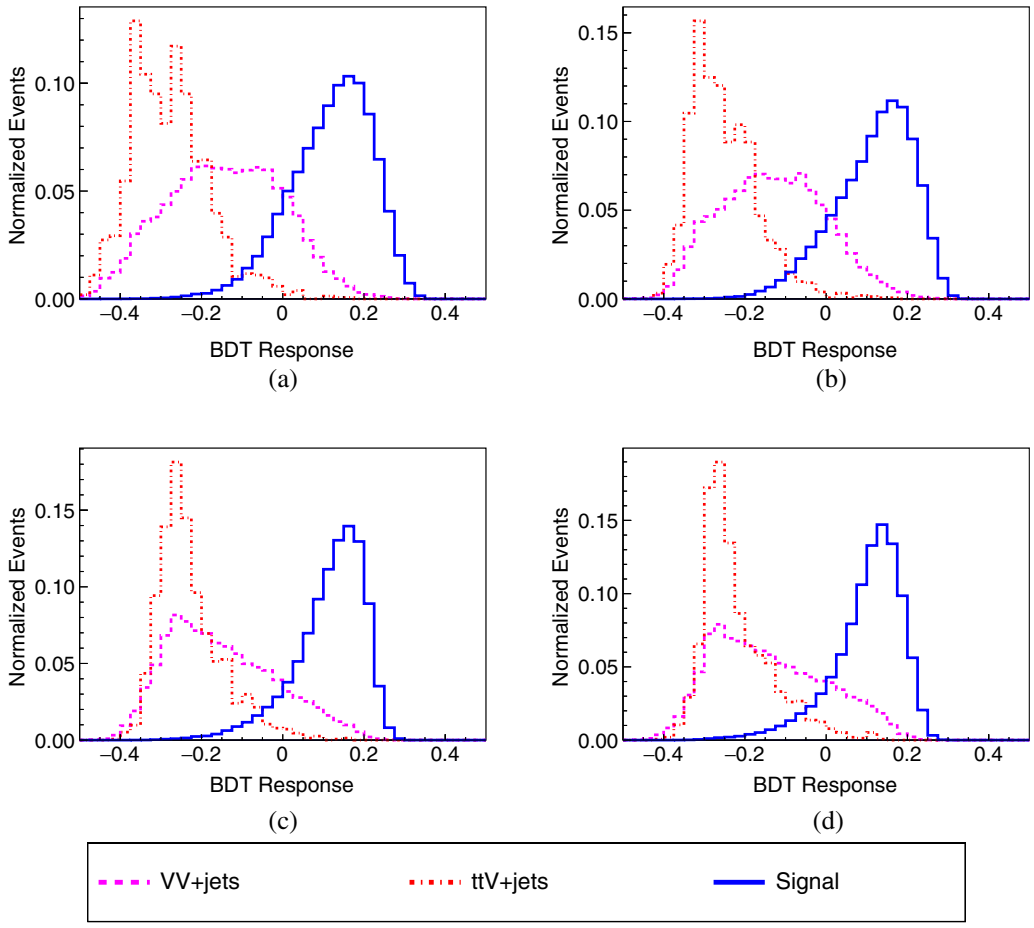

FIG. 6. Shape of the BDT discriminants for signal and backgrounds. The four plots are for four mass benchmarks: (m_χ, m_H) in GeV = (a) (20,160), (b) (20,170), (c) (60,160), and (d) (60,170).

integrated luminosity as high as 3000 fb^{-1} will be on the cards. In Table VIII we display a comparison of **S1** cross sections × branching ratios at $\sqrt{s} = 14$ and 13.6 TeV for a few benchmark points. The reduction in cross section for 13.6 TeV, as shown in Table VIII, is only (3-4)%.

Thus running LHC at a little bit lower energy, even keeping the same background contributions, costs the signal significance only marginally for the same beam luminosity. Also, the shape of the kinematic distributions does not significantly change either.

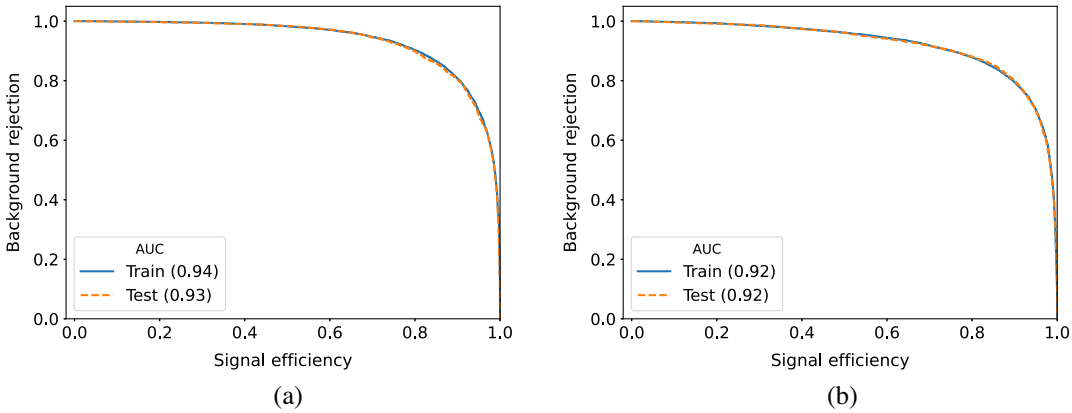

FIG. 7. ROC curves for (m_χ, m_H) in GeV: (a) (20,160) and (b) (60,170) with unweighted signal and background events with their AUC values.

TABLE VII. Summary of multivariate analysis (notations for the signals same as in Table III). Here we show the effect of BDT only for one coupling benchmark point $(Y_\ell, Y_q) = (0.005, 0.005)$.

Samples	Baseline cross section (fb)	Effective cross sections (fb) passing the best BDT score	Events $\mathcal{L} = 300$ fb^{-1}
$(20, 160) - (0.005, 0.005)$	0.845	0.453	135.98
$t\bar{t}Z +$ jets	0.141	0.001	0.11
$W^{\pm}Z +$ jets (31)	1.144	0.003	0.91
$ZZ +$ jets (41)	1.252	0.034	10.21
$(60, 170) - (0.005, 0.005)$	1.142	0.916	274.97
$t\bar{t}Z +$ jets	0.141	0.001	0.42
$W^{\pm}Z +$ jets (31)	1.144	0.031	9.39
$ZZ +$ jets (41)	1.252	0.173	52.06

How do the predictions of our scenario confront the existing run 2 LHC data? In Table IX, we display the signal cross sections times branching ratios at $\sqrt{s} = 13$ TeV along with the significance for $\mathcal{L} = 137.1$ fb^{-1} run 2 data collected by the CMS collaboration [26]. Interestingly, the numbers for run 2 are already quite encouraging, worth a dedicated study by the experimental groups.

VI. EFFECTS OF SYSTEMATIC UNCERTAINTIES WITH EXTENDED BENCHMARK SCENARIO

In Sec. V, we estimated the signal significance with four representative mass configurations of (m_χ, m_H), namely (20, 160/170) GeV and (60, 160/170) GeV. Using the cut based method and BDT, we obtained promising sensitivities to probe this channel. In this section, we give a broader

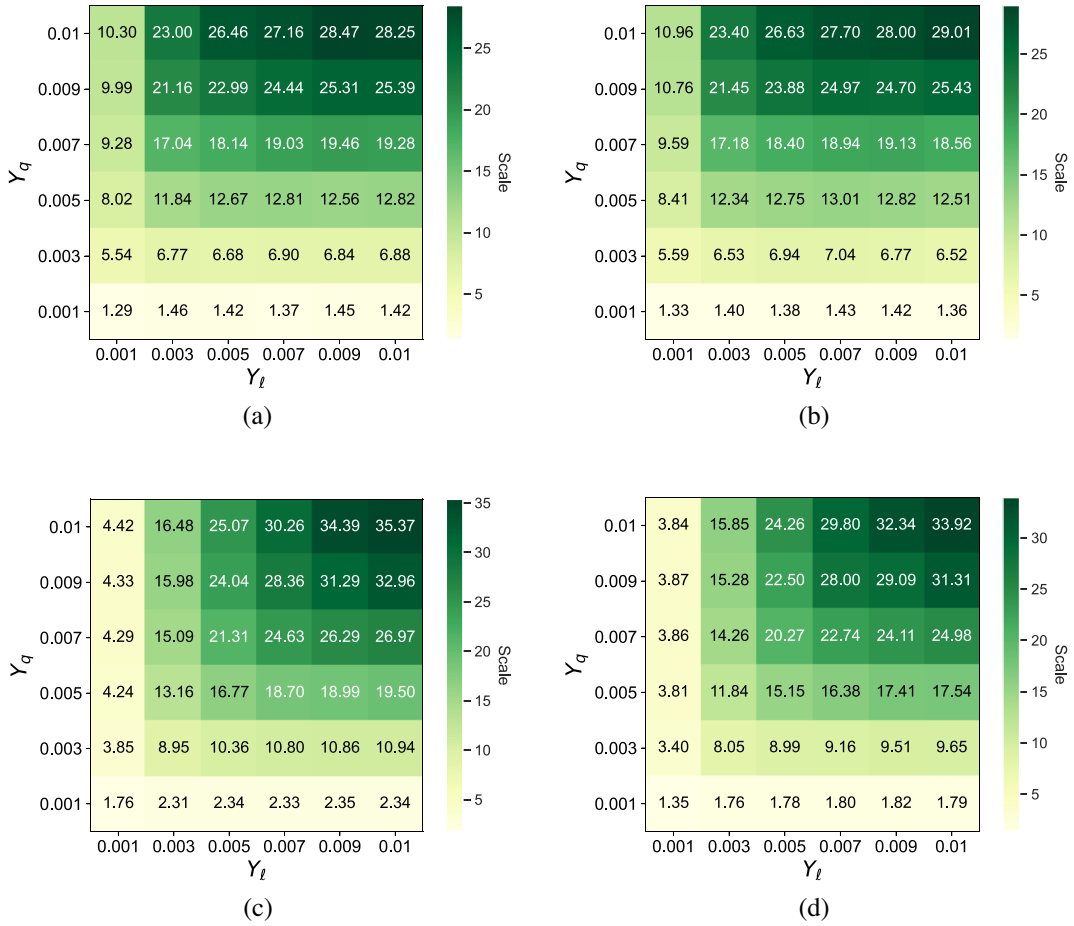

FIG. 8. Significance plots for the benchmark mass configurations at $\mathcal{L} = 300$ fb^{-1} after BDT. The four plots are for (m_χ, m_H) in GeV: (a) (20,160), (b) (20,170), (c) (60,160), and (d) (60,170).

TABLE VIII. **S1** cross sections × branching ratios for a few benchmark points at $\sqrt{s} = 14(13.6)$ TeV.

σ (fb)	$\sqrt{s} = 14(13.6)$ TeV			
(m_χ, m_H)	(20,160) GeV		(60,170) GeV	
	Y_q			
Y_ℓ	0.005	0.009	0.005	0.009
0.003	61.87(59.56)	158.03(152.42)	28.87(27.74)	42.97(41.47)
0.007	68.35(65.83)	208.77(201.03)	49.34(47.64)	115.89(111.31)

TABLE IX. **S1** cross sections × branching ratios (significance at $\mathcal{L} = 137.1$ fb^{-1}) for a few benchmark points at $\sqrt{s} = 13$ TeV.

σ(fb)($\mathcal{S}$)	$\sqrt{s} = 13$ TeV			
(m_χ, m_H)	(20,160) GeV		(20,170) GeV	
	Y_q			
Y_ℓ	0.007	0.01	0.007	0.01
0.007	118.58(12.86)	230.23(18.36)	98.40(12.80)	191.81(18.72)
0.01	121.33(13.03)	240.12(19.09)	100.34(12.54)	199.22(19.61)
(m_χ, m_H)	(60,160) GeV		(60,170) GeV	
0.007	92.78(16.65)	138.99(16.78)	75.66(15.37)	118.43(20.14)
0.01	107.97(18.23)	179.19(23.91)	87.65(16.88)	150.99(22.93)

perspective of our analysis employing an extended benchmark region as mentioned at the end of Sec. II, including possible impact of systematic uncertainties at High Luminosity (HL) option of the LHC.

In Fig. 9 we display the cross sections for a specific coupling combination, i.e., $Y_\ell = Y_q = 0.01$. Additionally, we choose $Y_\ell = Y_q = (0.003, 0.005, 0.01)$ to feel the impact of possible systematic uncertainties by varying m_H in the range 140–500 GeV and m_χ in the range 20–60 GeV. Clearly, the extended region thus cover the previously considered specific benchmark points analysed in Sec. V.

A comparison between Figs. 10(a) and 10(b) shows that for higher values of m_H (e.g., 250 GeV) a uniform cut on ΔR between μ' and τ_h can be applied regardless of the values of m_χ in the given range, while for relatively lighter m_H different values of m_χ require different ΔR cuts. The boost of the decay products from H is the crucial factor here. For $m_H \geq 250$ GeV, we therefore apply a uniform cut $\Delta R \leq 2$ (as the best possible choice) to improve the signal significance.

We now show the impact of including the background only systematic uncertainties by introducing a parameter (α) in the modified expression of signal significance $\mathcal{S} = S/\sqrt{S + B + (\alpha B)^2}$ [37]. In Fig. 11, we show the drop in signal significance by varying α in the range (0–0.2), and in Table X, we display the effects of systematics for a few representative benchmark points. While the significance drops with increasing systematics, for some parameter choices the situation still remains quite promising even after including a (10-20)% systematic uncertainties.

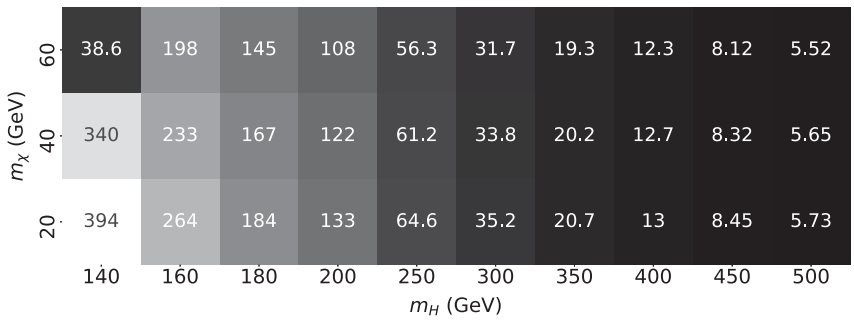

FIG. 9. **S1** Cross sections × branching ratios (fb) for additional mass benchmark points with $(Y_\ell, Y_q) = (0.01, 0.01)$.

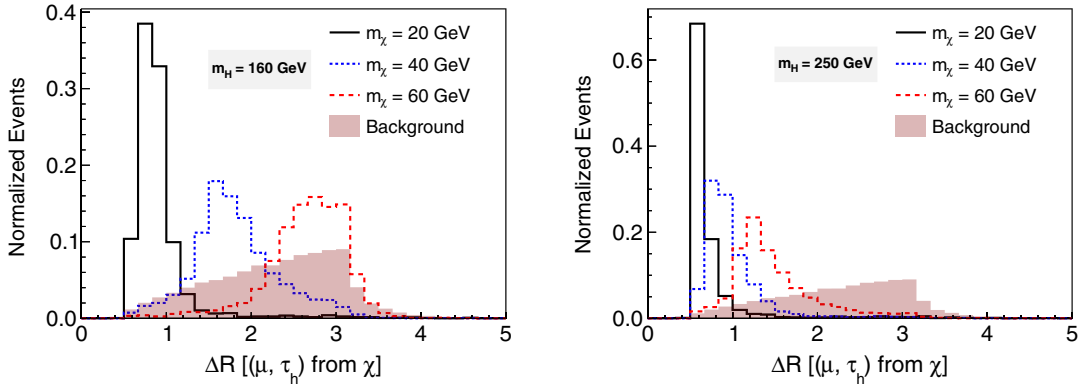

(a) (b)

FIG. 10. $\Delta R(\mu', \tau_h)$ for m_H (in GeV) = (a) 160 and (b) 250 with different choices of m_χ.

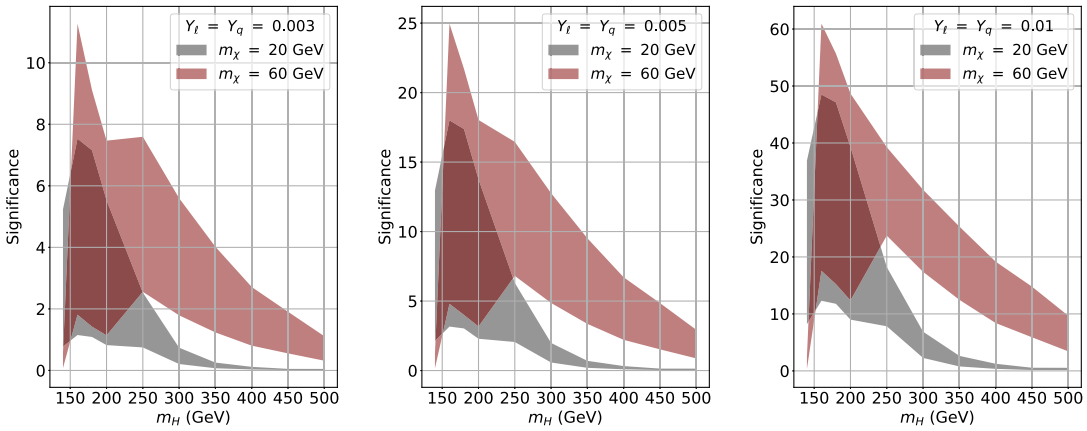

(a) (b) (c)

FIG. 11. Variation of significance with m_H for $m_\chi = 20$, 60 GeV and $Y_\ell = Y_q$ (a) 0.003, (b) 0.005, and (c) 0.01 by scanning α in the range (0–0.2) for $\mathcal{L} = 1000$ fb^{-1}. For each colored shade, the outer and inner edges correspond to $\alpha = 0$ and 0.2, respectively.

TABLE X. Signal significance for different benchmark scenarios for $\mathcal{L} = 1000$ fb^{-1} with 0%, 10%, and 20% systematic uncertainties on background contribution.

Significance ($\mathcal{S}$)	Systematic uncertainty = 0/10/20(%)		
		(Y_ℓ, Y_q)	
(m_χ, m_H) (GeV)	(0.003, 0.003)	(0.005, 0.005)	(0.01, 0.01)
(20,160)	7.53/2.22/1.15	18.01/6.05/3.16	48.51/22.53/12.31
(20,250)	2.53/1.33/0.75	6.31/3.58/2.05	18.22/12.56/7.83
(20,400)	0.12/0.06/0.03	0.32/0.16/0.09	1.25/0.64/0.36
(40,160)	8.79/2.64/1.37	20.61/7.15/3.74	53.79/26.17/14.43
(40,250)	8.07/4.74/2.75	17.63/11.89/7.37	41.18/34.77/25.48
(40,400)	1.51/0.77/0.43	3.91/2.11/1.99	12.33/7.79/4.56
(60,160)	11.26/3.49/1.81	24.95/9.12/4.79	60.94/31.42/17.56
(60,250)	7.59/4.42/2.56	16.45/11.07/6.81	39.26/32.79/23.74
(60,400)	2.71/1.43/0.81	6.71/3.84/2.2.1	19.17/13.38/8.41

VII. SUMMARY AND OUTLOOK

Any hypothetical Higgs-like state with SM-like couplings with ordinary matter and gauge fields would incur a serious constraint from its non observation at the LHC. What happens if the couplings are unconventional? In this analysis we explored whether rather light, $\mathcal{O}(10-100)$ GeV exotic CP-even (H) and CP-odd (χ) states having unusual Yukawa and gauge couplings could be observed through a resonance signature at the 14 TeV run of the LHC initially with 300 fb^{-1} data, where there is a possibility for a tenfold increase in luminosity (HL-LHC). Their Yukawa couplings are purely flavor off-diagonal, $H(\chi)ff'$, and there is no HVV (where $V \equiv Z$, W) interaction. To emphasize that our working hypothesis is not based on unrealizable wild assumptions, we point out that a broad class of flavor models based on discrete symmetry groups does predict such properties for nonstandard spin-0 states. Just with these two generic properties, these exotic states can avoid the conventional experimental constraints on their masses. Admittedly, to bypass the stringent constraints from D meson mixing an approximate adjustment between Y_q^H and Y_q^χ had to be innovated to yield results that are experimentally exciting. We have assumed $m_\chi \ll m_H$. We performed a detailed study with a few set of benchmark points: $m_H = (160, 170)$, $m_\chi = (20, 60)$, all in GeV. Subsequently, we include a wider range of benchmark points and incorporated possible systematic uncertainties to examine the expected signal significance. We displayed the significance as a function of those off-diagonal Yukawa couplings with quarks and leptons. Although the ancestral origin of these peculiar couplings may be traced, as mentioned before, in discrete flavor symmetry models, we remained agnostic about the UV picture of the new physics, and took a model independent view relying only on the overall gross pattern without committing to model-specific values of those Yukawa couplings.

The wisdom we gather from our analysis is that in general the multivariate analysis performs better than the traditional cut based method. As expected, larger Yukawa values show higher signal significance, and chances exist that the relatively larger couplings we chose as benchmark values, otherwise allowed by existing indirect constraints, can be ruled in or out with 300 fb^{-1} data at 14 TeV. Some of those couplings can even be tested at the upcoming 13.6 TeV run 3 data. In fact, even in the existing 13 TeV run 2 data, such exotic treasures might be hidden which require an in-depth experimental analysis for manifestation. To explore the smaller values of those couplings we cannot but rely on the HL-LHC. We admit that our analysis does not contain the following issues that experimental groups do pay attention to jet faking as τ_h and/or leptons, lepton charge misidentification, photon conversions into lepton pairs, uncertainties on luminosity and trigger efficiencies, etc. [38]. However, we have considered a linear-in-background systematic uncertainty to probe the signal sensitivity at the HL-LHC. Still, our results look quite promising and we hope that the initial steps we have taken in this paper would encourage the ATLAS and CMS exotica groups to pursue further in this direction.

ACKNOWLEDGMENTS

We thank S. Bhattacharya, T. Jha, and I. Chakraborty for discussions. We acknowledge the central computing facility of Saha Institute of Nuclear Physics for computational support.

[1] G. Altarelli and F. Feruglio, Discrete flavor symmetries and models of neutrino mixing, Rev. Mod. Phys. **82**, 2701 (2010).
[2] E. Ma, Non-Abelian discrete flavor symmetries, arXiv:0705.0327.
[3] H. Ishimori, T. Kobayashi, H. Ohki, Y. Shimizu, H. Okada, and M. Tanimoto, Non-Abelian discrete symmetries in particle physics, Prog. Theor. Phys. Suppl. **183**, 1 (2010).
[4] S. Pakvasa and H. Sugawara, Discrete symmetry and Cabibbo angle, Phys. Lett. **73B**, 61 (1978).
[5] G. Bhattacharyya, P. Leser, and H. Pas, Novel signatures of the Higgs sector from S3 flavor symmetry, Phys. Rev. D **86**, 036009 (2012).
[6] G. Bhattacharyya, P. Leser, and H. Pas, Exotic Higgs boson decay modes as a harbinger of S_3 flavor symmetry, Phys. Rev. D **83**, 011701 (2011).
[7] G. Bhattacharyya, I. de Medeiros Varzielas, and P. Leser, A Common Origin of Fermion Mixing and Geometrical CP Violation, and Its Test Through Higgs Physics at the LHC, Phys. Rev. Lett. **109**, 241603 (2012).
[8] C. Luhn, S. Nasri, and P. Ramond, The flavor group $\Delta(3n^2)$, J. Math. Phys. (N.Y.) **48**, 073501 (2007).
[9] Particle Data Group, Review of particle physics, Prog. Theor. Exp. Phys. **2020**, 083C01 (2020).
[10] F. J. Botella, G. C. Branco, M. Nebot, and M. N. Rebelo, Flavour changing Higgs couplings in a class of two Higgs doublet models, Eur. Phys. J. C **76**, 161 (2016).
[11] M. Lindner, M. Platscher, and F. S. Queiroz, A call for new physics: The muon anomalous magnetic moment and lepton flavor violation, Phys. Rep. **731**, 1 (2018).
[12] A. Alloul, N. D. Christensen, C. Degrande, C. Duhr, and B. Fuks, FeynRules 2.0—A complete toolbox for tree-level

phenomenology, Comput. Phys. Commun. **185**, 2250 (2014).
[13] J. Alwall, R. Frederix, S. Frixione, V. Hirschi, F. Maltoni, O. Mattelaer, H.-S. Shao, T. Stelzer, P. Torrielli, and M. Zaro, The automated computation of tree-level and next-to-leading order differential cross sections, and their matching to parton shower simulations, J. High Energy Phys. 07 (2014) 079.
[14] NNPDF Collaboration, Parton distributions for the LHC Run II, J. High Energy Phys. 04 (2015) 040.
[15] T. Sjöstrand, S. Ask, J. R. Christiansen, R. Corke, N. Desai, P. Ilten, S. Mrenna, S. Prestel, C. O. Rasmussen, and P. Z. Skands, An introduction to PYTHIA 8.2, Comput. Phys. Commun. **191**, 159 (2015).
[16] DELPHES 3 Collaboration, DELPHES 3, A modular framework for fast simulation of a generic collider experiment, J. High Energy Phys. 02 (2014) 057.
[17] M. Cacciari, G. P. Salam, and G. Soyez, The anti-k_t jet clustering algorithm, J. High Energy Phys. 04 (2008) 063.
[18] M. Cacciari, G. P. Salam, and G. Soyez, FastJet user manual, Eur. Phys. J. C **72**, 1896 (2012).
[19] J. M. Campbell, R. K. Ellis, and C. Williams, Vector boson pair production at the LHC, J. High Energy Phys. 07 (2011) 018.
[20] A. Kardos, Z. Trocsanyi, and C. Papadopoulos, Top quark pair production in association with a Z-boson at NLO accuracy, Phys. Rev. D **85**, 054015 (2012).
[21] C. Muselli, M. Bonvini, S. Forte, S. Marzani, and G. Ridolfi, Top quark pair production beyond NNLO, J. High Energy Phys. 08 (2015) 076.
[22] Particle Data Group, Review of particle physics, Phys. Rev. D **98**, 030001 (2018).
[23] ATLAS Collaboration, Search for neutral Higgs bosons of the minimal supersymmetric standard model in pp collisions at $\sqrt{s} = 8$ TeV with the ATLAS detector, J. High Energy Phys. 11 (2014) 056.
[24] CMS Collaboration, Search for additional neutral MSSM Higgs bosons in the $\tau\tau$ final state in proton-proton collisions at $\sqrt{s} = 13$ TeV, J. High Energy Phys. 09 (2018) 007.
[25] R. K. Ellis, I. Hinchliffe, M. Soldate, and J. J. van der Bij, Higgs Decay to $\tau^+\tau^-$: A possible signature of intermediate mass Higgs bosons at the SSC, Nucl. Phys. **B297**, 221 (1988).
[26] CMS Collaboration, Search for lepton-flavor violating decays of the Higgs boson in the $\mu\tau$ and $e\tau$ final states in proton-proton collisions at $\sqrt{s} = 13$ TeV, Phys. Rev. D **104**, 032013 (2021).
[27] D. Bardhan, A. Chakraborty, D. Choudhury, D. K. Ghosh, and M. Maity, Search for bottom squarks in the baryon-number violating MSSM, Phys. Rev. D **96**, 035024 (2017).
[28] A. Bhardwaj, P. Konar, T. Mandal, and S. Sadhukhan, Probing the inert doublet model using jet substructure with a multivariate analysis, Phys. Rev. D **100**, 055040 (2019).
[29] P. Konar, B. Mukhopadhyaya, R. Rahaman, and R. K. Singh, Probing non-standard $b\bar{b}h$ interaction at the LHC at $\sqrt{s} = 13$ TeV, Phys. Lett. B **818**, 136358 (2021).
[30] CMS Collaboration, Measurement of the t-Channel Single Top Quark Production Cross Section in pp Collisions at $\sqrt{s} = 7$ TeV, Phys. Rev. Lett. **107**, 091802 (2011).
[31] K. Albertsson *et al.*, Machine learning in high energy physics community white paper, J. Phys. Conf. Ser. **1085**, 022008 (2018).
[32] CMS Collaboration, Search for nonresonant Higgs boson pair production in the $b\bar{b}b\bar{b}$ final state at $\sqrt{s} = 13$ TeV, J. High Energy Phys. 04 (2019) 112.
[33] J. Quinlan, Simplifying decision trees, International Journal of Man-Machine Studies **27**, 221 (1987).
[34] A. Hocker *et al.*, TMVA—toolkit for multivariate data analysis, arXiv:physics/0703039.
[35] Y. Freund and R. E. Schapire, A decision-theoretic generalization of on-line learning and an application to boosting, J. Comput. Syst. Sci. **55**, 119 (1997).
[36] S. Fartoukh *et al.*, LHC configuration and operational scenario for Run 3, Report No. CERN-ACC-2021-0007, CERN, 2021, https://cds.cern.ch/record/2790409/files/CERN-ACC-2021-0007.pdf.
[37] G. Cowan, Discovery sensitivity for a counting experiment with background uncertainty, https://www.pp.rhul.ac.uk/$\sim$cowan/stat/medsig/medsigNote.pdf.
[38] CMS Collaboration, Performance of reconstruction and identification of τ leptons decaying to hadrons and ν_τ in pp collisions at $\sqrt{s} = 13$ TeV, J. Instrum. **13**, P10005 (2018).